

1 A general model for welding of ash particles in volcanic systems

2 validated using *in situ* x-ray tomography

3 Fabian B. Wadsworth<sup>1,2,3</sup>, Jérémie Vasseur<sup>3</sup>, Jenny Schaubert<sup>4</sup>, Edward W. Llewellyn<sup>1</sup>,

4 Katherine J. Dobson<sup>1</sup>, Tegan Havard<sup>1</sup>, Bettina Scheu<sup>3</sup>, Felix W. von Aulock<sup>4</sup>,

5 James E. Gardner<sup>5</sup>, Donald B. Dingwell<sup>2,3</sup>, Kai-Uwe Hess<sup>3</sup>, Mathieu Colombier<sup>3</sup>,

6 Federica Marone<sup>6</sup>, Hugh Tuffen<sup>7</sup>, Michael J. Heap<sup>8</sup>

7 <sup>1</sup>Department of Earth Sciences, Durham University, Durham, DH1 3LE, U.K. <sup>2</sup>Centre for Advanced Study, Ludwig-

8 Maximilians-Universität, Munich, Germany. <sup>3</sup>Department of Earth and Environmental Science, Ludwig-Maximilians-

9 Universität, Theresienstr. 41, Munich 80333, Germany. <sup>4</sup>School of Environmental Sciences, University of Liverpool, Jane

10 Herdman Building, Liverpool L69 3GP, U.K. <sup>5</sup>Department of Geological Sciences, Jackson School of Geosciences, 2305

11 Speedway Stop C1160, Austin, TX 78712-1692, U.S. <sup>6</sup>Swiss Light Source, Paul Scherrer Institut, 5232 Villigen PSI,

12 Switzerland. <sup>7</sup>Lancaster Environment Centre, Lancaster University, LA1 4YQ, U.K. <sup>8</sup>Institut de Physique du Globe de

13 Strasbourg (UMR 7516 CNRS), Université de Strasbourg, 5 rue René Descartes, F-67084, Strasbourg, France.

14 *sintering; porosity; synchrotron; surface tension; tomography; tuffisite; jet engine; obsidian*

15 corresponding author: [fabian.b.wadsworth@durham.ac.uk](mailto:fabian.b.wadsworth@durham.ac.uk)

16

17 **Abstract:**

18 **Welding occurs during transport and deposition of volcanic particles in diverse settings,**  
19 **including pyroclastic density currents, volcanic conduits, and jet engines. Welding rate**  
20 **influences hazard-relevant processes, and is sensitive to water concentration in the melt.**  
21 **We characterize welding of fragments of crystal-free, water-supersaturated rhyolitic**  
22 **glass at high temperature using *in-situ* synchrotron-source x-ray tomography.**  
23 **Continuous measurement of evolving porosity and pore-space geometry reveals that**  
24 **porosity decays to a percolation threshold of 1 – 3 vol.%, at which bubbles become**  
25 **isolated and welding ceases. We develop a new mathematical model for this process that**  
26 **combines sintering and water diffusion, which fits experimental data without requiring**  
27 **empirically-adjusted parameters. A key advance is that the model is valid for systems in**  
28 **which welding is driven by confining pressure, surface tension, or a combination of the**  
29 **two. We use the model to constrain welding timescales in a wide range of volcanic**  
30 **settings. We provide user-friendly tools, written in Python™ and in Excel™, to solve for**  
31 **the evolution of porosity and dissolved water concentration during welding for user-**  
32 **defined initial conditions.**

33

34 Key points:

- 35 (1) First *in situ* determination of the welding rates of hydrous magma.  
36 (2) A new mathematical model that couples volatile mass transfer with welding kinetics.  
37 (3) This work provides a model relevant for ignimbrite and tuffisite welding

38        **1. Introduction**

39 Magma fragments into particles during explosive volcanic activity. Subsequent welding of  
40 these particles can occur at the base of hot pyroclastic density currents (Walker 1983;  
41 Branney et al. 1992), at the walls of volcanic conduits (Gonnermann and Manga 2003; Rust  
42 et al. 2004; Gardner et al. 2017), in tuffisite veins (Tuffen et al. 2003; Kendrick et al. 2016;  
43 Gardner et al. 2018), in the hot zone of jet engines (Giehl et al. 2016), and when lightning  
44 strikes volcanic ash in the air or on the ground (Cimarelli et al. 2017; Mueller et al. 2018).  
45 Despite this wide range of welding scenarios, there has been little work on the physics of  
46 welding of volcanic droplets, beyond simple empirical, semi-empirical, or scaling approaches  
47 (Friedman et al. 1963; Riehle 1973; Sparks et al. 1999; Quane and Russell 2005a; Russell and  
48 Quane 2005; Vasseur et al. 2013; Wadsworth et al. 2014).

49        Welding involves a reduction of inter-particle pore space (Branney and Kokelaar  
50 1992; Sparks et al. 1999; Quane and Russell 2005a; Vasseur et al. 2013). Porosity is therefore  
51 a convenient metric for tracking the degree of welding, and has been used to rank the ‘grade’  
52 of a welded deposit (Quane and Russell 2005b; Wright and Cashman 2014). Theoretical  
53 models for the evolution of porosity as a function of time in a welding system have been  
54 proposed (Frenkel 1945; Mackenzie and Shuttleworth 1949) but they do not account for the  
55 complexities of welding in magmatic systems, which include non-isothermal behavior,  
56 disequilibrium of dissolved volatile species, and the effect of a confining pressure that pushes  
57 the particles together. Non-isothermal behavior is important because welding in nature may  
58 occur as the particles cool (e.g. at conduit margins, within ejected ballistic bombs, or in  
59 ignimbrites) or follow more complex heating and cooling pathways (e.g. in a jet engine).  
60 Disequilibrium of volatile species – particularly of water – is important because the solubility  
61 changes as the pressure and temperature environment of the particles changes, driving  
62 diffusion in or out of the particles during welding (Sparks et al. 1999; Gardner et al. 2018). In

63 the case of water, this has a strong impact on the viscosity of the particle (Hess and Dingwell  
64 1996) affecting welding rate (Grunder et al. 2005; Gardner et al. 2018, 2019). Confining (or  
65 lithostatic) pressure resulting, for example, from the weight of aggrading particles at the base  
66 of a pyroclastic density current, is important because it provides a stress that pushes the  
67 droplets together, accelerating welding. Previous theoretical and quantitative models for  
68 welding have focused on cases where welding is driven by surface tension alone (Wadsworth  
69 et al. 2016) or, where pressure is considered, have relied on scaling arguments (Sparks et al.  
70 1999) or purely empirical correlations (e.g. Riehle 1973).

71 We develop a general and versatile mathematical framework for welding that can be used  
72 to predict the textural evolution of a welding pack of particles in a wide range of natural  
73 settings. We perform and analyze experiments conducted under non-isothermal,  
74 disequilibrium conditions to validate the model.

75

## 76 **2. A theoretical model for droplet welding dynamics**

### 77 **a. Viscous welding under arbitrary pressure**

78 Previous work on non-volcanic welding (or ‘sintering’) of spherical particles has shown that  
79 in the viscous state (i.e. when particles are droplets), surface-tension-driven welding is well  
80 described by a ‘vented bubble model’, in which the inter-droplet porosity is abstracted as a  
81 system of spherical bubbles in liquid shells, which are ‘vented’ so that the gas can escape as  
82 the bubbles shrink (Mackenzie and Shuttleworth 1949; Wadsworth et al. 2016). The  
83 geometric assumptions of the vented bubble model are most valid for highly polydisperse  
84 particle distributions (Wadsworth et al. 2017b) of the sort typical in nature, and the  
85 approximation becomes increasingly accurate as welding progresses because, as the droplets  
86 coalesce, the microstructural geometry continuously diverges from ‘droplet-like’ towards  
87 ‘bubble-like’ – that is, there is a topological inversion of the pore space (Wadsworth et al.

88 2017a). We start from the assumption that the vented bubble model also applies to initially-  
 89 angular particles. The conceptual steps in the geometric abstraction from an ash pack to a  
 90 system of vented bubbles are shown in Figure 1.

91 We extend the vented bubble model to include a confining pressure that acts  
 92 alongside surface tension stress to drive welding, where we use the term *confining* pressure to  
 93 refer to an isotropic pressure acting to push the particles together – equivalently, when  
 94 viewing the particles as viscous droplets, an isotropic pressure in the continuous liquid phase  
 95 of the coalescing droplets. In their supplementary material, Wadsworth et al. (2016) derive  
 96 the vented bubble model from the model of Prousevitch et al. (1993) for bubble growth in  
 97 magma by setting the bubble pressure inside the associated liquid shell to be equal to the gas  
 98 pressure outside the shell at all times. Here, we relax that assumption, and instead set the  
 99 pressure difference to a value  $\Delta P$ . Neglecting inertia, the full equation for the inter-droplet  
 100 porosity  $\phi$  with time  $t$  is then

$$\frac{d\phi}{dt} = -\frac{3\Delta P}{4\mu}\phi - \frac{3\Gamma}{2\mu a_i}\left(\frac{\phi_i}{1-\phi_i}\right)^{1/3}\phi^{2/3}(1-\phi)^{1/3}, \quad \text{Eq. 1}$$

102  
 103 where  $\Delta P$  is the difference between the confining pressure on the liquid droplets  $P_l$  and the  
 104 pressure of the interstitial gas  $P_g$ , such that  $\Delta P = P_l - P_g$ ,  $\mu$  is the particle viscosity,  $\Gamma$  is the  
 105 interfacial tension between the particles and the gas,  $a_i$  is the initial size of the bubble, and  $\phi_i$   
 106 is the initial porosity when welding starts. A derivation of Eq. 1 from the Rayleigh-Plesset  
 107 equation is given in the Supplementary Information.

108 Eq. 1 can be cast in dimensionless form by normalizing time to a characteristic  
 109 capillary timescale  $\lambda = \mu a_i / \Gamma$ , such that  $\bar{t} = t / \lambda$ , normalizing pressure to a capillary

110 pressure scale  $P_c = 2\Gamma/a_i$ , such that  $\bar{P} = \Delta P/P_c$ , and normalizing porosity to its initial value,  
 111 such that  $\bar{\phi} = \phi/\phi_i$ , yielding

112

$$\frac{d\bar{\phi}}{d\bar{t}} = -\frac{3}{2} \left[ \bar{P}\bar{\phi} + \left( \frac{1 - \phi_i\bar{\phi}}{1 - \phi_i} \right)^{1/3} \bar{\phi}^{2/3} \right], \quad \text{Eq. 2}$$

113

114 where a bar above a parameter denotes that it has been rendered dimensionless. The first term  
 115 within the square brackets represents the contribution of the confining pressure, the second  
 116 term represents the contribution of the capillary (Laplace) pressure.

117 The dimensionless time  $\bar{t}$  can be generalized to account for non-isothermal  
 118 temperature–time history, which is especially useful for natural magmatic scenarios. This is  
 119 achieved by accounting for the change in viscosity  $\mu$  as temperature varies, via

120

$$\bar{t} = \frac{t}{\lambda} = \frac{\Gamma}{a_i} \int_{t_i}^t \frac{1}{\mu} dt \quad \text{Eq. 3}$$

121

122 where  $t_i$  is the time at which the welding process starts. In casting Eq. 3 this way, we assume  
 123 that  $\Gamma$  is a constant, independent of time during welding. In reality,  $\Gamma$  is dependent on both  
 124 water concentration and temperature, however, variations in surface tension are negligible  
 125 compared with variations in liquid viscosity arising from the effects of both temperature and  
 126 water concentration (discussed later). Together, Eqs 2 & 3 represent a universal description  
 127 of isotropic, viscous particle welding, derived from micromechanical first principles. In the  
 128 case where  $\bar{P} = 0$ , this approach has been validated against experimental data across a large  
 129 range of temperatures (Wadsworth et al. 2016). While other models exist, they are either less  
 130 easy to use, requiring a switch-point between two competing processes (Prado et al. 2001), or

131 they rely on bulk properties of the system, which have to be empirically determined and are  
132 therefore less general as they are not constructed from the micromechanics involved  
133 (Olevsky 1998; Quane and Russell 2005a).

134 The parameter  $a_i$  can be difficult to measure, or even define, for what is a complex,  
135 interconnected pore network (Figure 1). We use a relationship between  $a_i$  and the distribution  
136 of particle sizes  $F(R)$  in a pack of particles or droplets (Lu and Torquato 1992), which is  
137 described in detail elsewhere (Wadsworth et al. 2016, 2017b). The relationship relies on  
138 knowledge of  $\phi_i$ , and the moments of the distribution of  $R$ , denoted  $\langle R^n \rangle$ , which can be  
139 grouped into a polydispersivity factor  $S = \langle R \rangle \langle R^2 \rangle / \langle R^3 \rangle$ . The output from this is a pore size  
140 distribution  $f(a_i)$  that relates to the particle size distribution  $F(R)$  and  $\phi_i$ , and is described in  
141 the Supplementary Information along with an account of how this is used in conjunction with  
142 Eqs 1-2 using convolution techniques (Wadsworth et al. 2017b).

143

#### 144 **b. Accounting for diffusion of volatiles during welding**

145 In the model formulation above, the viscosity  $\mu$  is assumed to be dependent on temperature,  
146  $T$ , only. However, viscosity also depends on the concentration of water dissolved in the melt,  
147 which, in nature, may vary during welding. Volcanic particles formed at fragmentation may  
148 be super-saturated in dissolved water (Giachetti and Gonnermann 2013), and that super-  
149 saturation can grow as the particles ascend rapidly to lower pressures up-conduit without time  
150 to fully re-equilibrate (Gardner et al. 2017). Similarly, the solubility of water increases as the  
151 particles cool, which may cause them to re-hydrate (McIntosh et al. 2014; Ryan et al. 2015).  
152 Mass diffusion of water in or out of particles may occur on timescales similar to the timescale  
153 of welding (Sparks et al. 1999; Gardner et al. 2017, 2018, 2019); consequently, we anticipate  
154 that diffusion of water can affect the rate of welding through its impact on melt viscosity.

155 In order to account for diffusion, we must define the geometry of the internal welding  
 156 system. The internal geometry of welding systems is complex and evolves from an initial  
 157 state of particles in a gas continuum, to bubbles isolated in a liquid continuum. A rigorous  
 158 solution for mass diffusion through this evolving geometry would require an approach that  
 159 explicitly resolves both the fluid motion and the diffusion. However, as for the welding  
 160 model, we simplify the problem by abstracting the geometry. For the purposes of diffusion  
 161 modeling we assume that the particles remain spherical and simply apply Fick's 2<sup>nd</sup> law in  
 162 spherical coordinates,

$$\frac{\partial C}{\partial t} = \frac{1}{r^2} \frac{\partial}{\partial r} \left( r^2 D \frac{\partial C}{\partial r} \right),$$

Eq. 4

164  
 165 where  $C$  is the concentration of water in the melt particle,  $D$  is its diffusivity (which depends  
 166 on temperature and local water concentration), and  $r$  is the radial position from the particle  
 167 center. We adopt the assumption that the initial concentration of dissolved water  $C_i$  is  
 168 uniform throughout the particle at the onset of welding, giving the initial condition  $C = C_i$  for  
 169 all  $r$  at  $t = 0$ . At all later times the water concentration at the surface of the particle is given  
 170 by the equilibrium solubility  $C_e$  at the current conditions of gas pressure  $P_g$  and temperature  
 171  $T$ , giving the boundary condition  $C = C_e(t)$  at  $r = R$  for  $t > 0$ . We define a zero-flux  
 172 boundary condition at the center of the particle:  $\partial C / \partial r = 0$  at  $r = 0$ .

173 To account for the effect of variable water concentration in the particle we determine a  
 174 spatial average by integrating  $C$  over  $0 < r < R$ ; this integral is  $\langle C \rangle = \int_0^1 C d\bar{r}$ , where  
 175  $\bar{r} = r/R$ . We then use  $\langle C \rangle$  to compute an average viscosity  $\langle \mu \rangle$  which is used in Eqs 1-3 in  
 176 place of  $\mu$ . This approach results in an effective coupling between the diffusion model (Eq. 4)  
 177 and the welding model (Eqs 1-3). In the Supplementary Information, we describe the



178 numerical solution of these equations in detail. We note here that our assumption of spherical  
179 particles undergoing diffusion of volatiles may be invalid at large polydispersivity for cases  
180 where the smallest particles are in equilibrium while the largest particles are far from  
181 equilibrium. This is discussed elsewhere (Gardner et al. 2019).

182

### 183 **3. Experimental validation: materials and methods**

184 Our starting material is a metaluminous, tholeiitic natural rhyolitic glass collected from  
185 Hrafninnuhryggur, Krafla (Iceland). We crushed the obsidian to a powder using an agate  
186 mortar and pestle and then crushed the resultant chips to a fine powder using a concussion  
187 ball mill for short durations to prevent the sample heating significantly. The powder was  
188 sieved to  $< 125 \mu\text{m}$  diameter pieces and the size distribution was measured using a Beckman  
189 Coulter LS<sup>TM</sup> 230 laser refraction particle size analyzer with the measuring range 0.375 –  
190 1000  $\mu\text{m}$  diameter. The particle size distribution is given in the Supplementary Information,  
191 and has a mean radius  $\langle R \rangle = 2.2 \times 10^{-5} \text{ m}$ .

192 Using a Netzsch Pegasus 404c device for simultaneous thermal analysis, we  
193 determined the dissolved volatile concentration that is excess (above solubility) at up to  
194 1325 K to be  $C_i = 0.15 \pm 0.02 \text{ wt.}\%$ , by the relative loss of mass during heating, consistent  
195 with Tuffen and Castro (2009). This determination was performed on single chips ( $n = 6$ )  
196 from within a few millimeters of the sub-sample of the glass block that was used throughout  
197 this study.

198 To solve the governing equations given in our model, we require a parameterization  
199 for  $D$ ,  $\mu$ , and  $C_e$  relevant to the material in question. We use models relevant to the  
200 metaluminous rhyolites (Hess and Dingwell 1996; Liu et al. 2005; Zhang and Ni 2010)

201

$$\log_{10}(\mu) = -3.545 + 0.833 \ln(C) + \frac{9601 - 2368 \ln(C)}{T - 195.7 - 32.25 \ln(C)}$$

$$D = C \exp \left[ -18.1 + 0.001888 P_l - \left( \frac{9699 + 3.626 P_l}{T} \right) \right] \quad \text{Eq. 5}$$

$$C_e = \frac{354.941 P_w^{0.5} + 9.623 P_w - 1.5223 P_w^{1.5}}{T} + 0.0012439 P_w^{1.5}$$

202

203 where  $P_w$  is the partial pressure of water in the interstitial gas phase, and the coefficients  
 204 given are valid when  $T$  is in K,  $P_l$  and  $P_w$  are in MPa, and  $C$  and  $C_e$  are in wt.%. In the  
 205 Supplementary Information we independently verify  $\mu(T)$  for our material using a parallel  
 206 plate compression method (Hess et al. 2007), a calorimetric method using a shift factor of  
 207 10.4 (Gottsmann et al. 2002), and a micropenetration method (Hess et al. 1995), which all  
 208 demonstrate internal consistency, as well as matching the prediction of Eq. 5 for the  
 209 measured  $C_i$ . We take a value  $P_w = P_l \alpha$  with  $\alpha = 0.2$ , representing the typical humidity  
 210 pressure in a laboratory furnace. Finally, we use  $\Gamma = 0.3 \text{ N.m}^{-1}$ .

211 We performed two sets of *in situ* high temperature experiments, which used different  
 212 methods to image the evolution of a welding pack of obsidian powder, lightly pressed into a  
 213 free-standing cylinder with 3 mm diameter: (1) synchrotron-source x-ray tomography,  
 214 providing continuous 3-dimensional microstructural data; and (2) optical dilatometry,  
 215 providing bulk sample volume changes only. The first set of experiments were performed at  
 216 the TOMCAT beamline of the Swiss Light Source at the Paul Scherrer Institute. Cylinders of  
 217 obsidian powder were loaded into the imaging window of the x-ray beam path. We used a  
 218 laser system (Fife et al. 2012) to heat an alumina sleeve (muffle) placed over the samples,  
 219 thus heating the obsidian pack indirectly. The temperatures measured by a pyrometer were  
 220 calibrated by comparing the *in situ* welding of a well-studied sample of monodisperse glass  
 221 beads with *ex situ* characterization of the same process (Wadsworth et al. 2016), resulting in a  
 222 continuous correction for  $T$ , and confirming that temperature gradients on the sample scale

223 were negligible. Full 3-dimensional tomographs were collected at  $5.5 \times 10^{-3}$  Hz with a  
224 spatial resolution of  $1.6 \mu\text{m}$ . The second set of experiments were performed using a Hesse  
225 Instruments EM-201 optical dilatometer, which continuously records the silhouette of the  
226 sample during heating at 1 Hz. Volume is determined from the silhouette as the solid of  
227 revolution.

228 The experiments covered a wide range of conditions, including isothermal  
229 experiments at temperatures of  $1050 - 1500$  K, and linear heating ramps at rates of  $0.04 -$   
230  $0.25 \text{ K} \cdot \text{s}^{-1}$ . The data from optical dilatometry are confined to porosity  $\phi(t)$ , while the  
231 tomography provides 3-dimensional data that are used to measure both the total porosity  
232  $\phi(t)$ , and the porosity that is connected across the sample (or segmented domain)  $\phi_p(t)$ .  
233 After the heating experiments, we repeated the thermal analysis step on a few sub-samples,  
234 and no mass loss was observed, demonstrating the samples did equilibrate volatiles during  
235 the *in situ* experiments.

236 Supplementing our datasets collected at relatively low  $C_i$  and a small difference  
237 between  $C_i$  and  $C_e$  (small initial supersaturation), we re-analyse the data from Gardner et al.  
238 (2018) and Gardner et al. (2019). These data were collected at high  $P_g$  such that the  
239 equilibrium water concentration is also high. These data also include particles that hydrate  
240 and particles that de-hydrate while also welding.

241 All of the above experiments were conducted without confining pressure, hence  $\bar{P} \approx 0$ , a  
242 situation typical of small-scale laboratory settings. In order to examine the effect of  $\bar{P} > 0$ ,  
243 we use data for welding Pyrex<sup>TM</sup> glass presented previously (Friedman et al. 1963). In those  
244 experiments the glass was crushed to a particle size around  $100 - 250 \mu\text{m}$  (not specified  
245 exactly), and welded under a uniaxial liquid pressure of  $P_l = 1.52 \times 10^6$  Pa and  $P_l = 3.63 \times$   
246  $10^6$  Pa at temperatures  $883 - 943$  K. We re-analyze these data using our model. While the  
247 same authors provide data for rhyolite particle welding (Friedman et al. 1963), some doubt

248 exists as to the exact pressures used (Sparks et al. 1999) so we choose not to reanalyze those  
249 data.

250

#### 251 **4. Results, data analysis and model validation**

252 *In situ* tomography allows us to render the evolving internal pore space of the samples in 3-  
253 dimensions through the welding process. Figure 2 shows a typical experimental result. The  
254 pore space is initially fully interconnected, and has a complex geometry between the angular  
255 glass fragments. As we heat the sample, the glass particles relax to liquid droplets at high  
256 temperature, and the droplet–droplet contacts weld. The porosity decreases with time  
257 smoothly and monotonically, and the rate at which it decreases depends strongly on  
258 temperature (in the isothermal experiments) or heating rate (in the non-isothermal  
259 experiments). The connectivity of the pore space drops during welding from fully connected  
260 at the start ( $\phi_p/\phi = 1$ ), to fully closed at volume equilibrium ( $\phi_p/\phi = 0$ ). The porosity at  
261 which the connectivity drops to zero is the percolation threshold porosity  $\phi_c$  below which the  
262 system is impermeable. We determine this from our experiments as  $\phi_c = 0.02 \pm 0.019$ ,  
263 which agrees with theory, simulations (Elam et al. 1984; Vasseur and Wadsworth 2017), and  
264 experiments (Wadsworth et al. 2016) in other welding droplet or overlapping sphere systems.  
265 This value is far lower than the percolation threshold for bubbly systems, as has previously  
266 been noted for the internal geometry of welding systems (Vasseur and Wadsworth 2017).

267 In Figures 2g & 3, we compare the results for the *in situ* x-ray tomography and optical  
268 dilatometry experiments with the model presented in section 2. For these unconfined  
269 laboratory-scale tests, the value of  $\bar{P}$  is effectively 0. For the isothermal experiments we solve  
270 Eq. 2 with  $\bar{P} = 0$ , accounting for the diffusion of water out of the particles during welding  
271 via Eqs 3 & 4 (Figures 3a & 3b). For the non-isothermal experiments we additionally account  
272 for temperature change via Eq. 3 (Figure 3c). In both cases, we find good agreement and a

273 reasonable collapse of the data to the model. This result highlights that, in these experiments,  
274 welding rates are influenced by temperature and volatile content, both of which control the  
275 particle viscosity and can evolve on the same timescale as the welding; hence, they must be  
276 solved explicitly (Eqs 3 & 4). Welding rate also depends on particle size distribution,  
277 interfacial tension, and the initial porosity of the packed particles. Particle angularity may  
278 subtly affect both the diffusion rate and the sintering rate when compared with the model,  
279 which is based on idealised spherical particles, but, given the good agreement between model  
280 and data, this effect does not appear to be of first-order.

281 The experimental validation of our simple model for  $\bar{P} = 0$  appears to be successful. To  
282 extend this to conditions where  $\bar{P} > 0$ , we re-analyse the results from Friedman et al. (1963)  
283 in which anhydrous glass was heated under pressure. In the Supplementary Information we  
284 give a detailed description of the methods used in Friedman et al (1963), but note here that  
285 Eqs 1 and 2 are valid in their experiments. We assume that the uniaxial nature of their applied  
286 loads can be accounted for using the Trouton ratio, such that our model for isotropic  
287 pressurization can be adapted to uniaxial conditions. For their anhydrous experiments,  
288 conducted at  $\bar{P} = 100$ , we apply Eq. 2 directly. We find good agreement across a wide range  
289 of temperature (Figure 4), validating our model up to naturally relevant pressures and across  
290 the regime boundary  $\bar{P} = 1$ . These conditions represent the state where the volcanic particles  
291 are under pressure, but the interconnected gas phase between the particles remain un-  
292 pressurized, which is a typical scenario for larger systems in nature. We show that, in this  
293 case, the time required for welding to complete is reduced by the elevated confining pressure,  
294 as implied by Eq. 2 (note how the data collapse to a model curve to the left of the  $\bar{P} =$   
295 0 curve in Figure 4, and are therefore welding more rapidly).

296

## 297 5. Discussion

298 **a. Validity of the welding model**

299 The welding model agrees well with experimental data across a wide range of conditions,  
300 validating the model for application to welding systems: 1) with and without applied  
301 pressure; 2) under isothermal and non-isothermal conditions; 3) in which dissolved water is  
302 in equilibrium or disequilibrium with ambient pressure and temperature conditions. Thus the  
303 model is sufficiently general to capture most of the essential features of welding scenarios in  
304 magmatic and volcanic systems. There are, however, two limitations. Firstly, the model does  
305 not apply directly to welding under high shearing stress. We do use experimental data in  
306 which welding particles are under uniaxial compression (Friedman et al. 1963), such that the  
307 anisotropy of the pressure applied results in shear stresses internal to the sample (c.f. uniaxial  
308 experiments in Quane and Russell 2005; Heap et al. 2015), which we account for via the  
309 Trouton ratio. This gives us some confidence that, under minor local shearing within a  
310 system that is loaded anisotropically, our model is valid. Nonetheless, we note that validation  
311 for shearing systems requires future systematic study over a larger range of better constrained  
312 shear stress. This limitation means that our model does not, for example, explicitly predict the  
313 formation of fiammé in welded ignimbrites. Secondly, the model assumes that interstitial gas  
314 escapes freely from the welding system, and does not apply when gas escape is significantly  
315 hindered by the permeability of the connected pore network. We can determine the  
316 conditions under which this second limitation is important.

317 The characteristic lengthscale beyond which a viscous system is permeability-limited  
318 is the compaction length  $L_c = (k_r \mu / \mu_g)^{1/2}$  (Michaut et al. 2009; Kennedy et al. 2016),  
319 where  $k_r$  is a reference permeability and  $\mu_g$  is the gas viscosity. If we normalize our system  
320 length by  $L_c$  we have

321

$$\bar{L} = \frac{L}{L_c} \approx L \sqrt{\frac{\mu_g}{k_r \mu}}. \quad \text{Eq. 6}$$

322

323 If  $\bar{L} \gg 1$ , permeability is a rate-limiting parameter, with the consequence that  $P_g$  may rise in  
 324 parts of the system and affect the welding rate (because the welding rate depends is sensitive  
 325 to  $P_c - P_g$ ); this regime is termed *compaction welding*. If  $\bar{L} \ll 1$ , gas escape can occur more  
 326 rapidly than welding occurs and the process is not hindered by sluggish gas escape. The  
 327 analysis presented via Eqs 1-4 is therefore valid in the regime  $\bar{L} \ll 1$ .

328

329 **b. Welding regimes in nature**

330 The dimensionless length  $\bar{L}$  discriminates between regimes in which welding is or is not  
 331 limited by permeable outgassing of the interstitial gas phase. For the non-limited regime  
 332 ( $\bar{L} \ll 1$ ) in which our welding model is valid, we can also discriminate between regimes in  
 333 which welding is dominated by confining pressure (*pressure welding*), or by capillary  
 334 pressure arising from the surface tension (*capillary welding*). From Eq. 2, we see that the  
 335 confining pressure term dominates the capillary pressure term when

336

$$\begin{aligned} \bar{P} &\gg \left( \frac{1 - \phi_i \bar{\phi}}{\bar{\phi} - \bar{\phi} \phi_i} \right)^{1/3} && \text{pressure welding,} \\ \bar{P} &\ll \left( \frac{1 - \phi_i \bar{\phi}}{\bar{\phi} - \bar{\phi} \phi_i} \right)^{1/3} && \text{capillary welding.} \end{aligned} \quad \text{Eq. 7}$$

337

338 The dependence on the porosity (via  $\bar{\phi}$ ) arises because capillary stress always tends towards  
 339 infinity as bubble radius tends towards zero, such that a system that starts in the pressure  
 340 welding regime may end in the capillary regime with no change in the ambient conditions.  
 341 The value of the terms on the right hand side of Eq. 7 is equal to unity at the start of welding

342 so, in practice we use  $\bar{P} \gg 1$  and  $\bar{P} \ll 1$  to discriminate between pressure and capillary  
343 welding regimes.

344         Given these constraints ( $\bar{P}$  and  $\bar{L}$ ), we can assess the regimes covered by some typical  
345 volcanic welding scenarios. For any situation in which welding might occur, we therefore  
346 need to know  $\mu$ ,  $R_i$ ,  $L$ , and  $\Delta P$  (for simplicity, we take a constant  $\Gamma = 0.3 \text{ N}\cdot\text{m}^{-1}$   
347 (Wadsworth et al. 2016),  $\mu_g \approx 10^{-5} \text{ Pa}\cdot\text{s}$ , and  $k_r = k_i \approx 7 \times 10^{-12} \text{ m}^2$  for packed particles  
348 (Wadsworth et al. 2017a)). For these dimensional considerations we assume that  $a_i = R_i$ ,  
349 because there is usually insufficient information provided to compute  $a_i$  explicitly, and we  
350 justify this by noting that these values are typically of the same order of magnitude  
351 (Wadsworth et al. 2016). In Table 1 we give a compilation of estimated values for these  
352 parameters gathered from well-studied welded ignimbrites, tuffisites, welded jet engine  
353 deposits, and welded obsidian pyroclasts. In each case, these parameters are converted to a  
354 quantitative range of  $\bar{P}$  and  $\bar{L}$  that represents the initial conditions for that particular system,  
355 and plotted in Figure 5. In the case of tuffisites from Volcán Colima, we use the values of  
356 particle (droplet) viscosity from Kendrick et al. (2016) which incorporate the effect of  
357 crystallinity.

358         We find that very few systems are in the  $\bar{L} \gg 1$  (permeability limited) regime.  
359 Exceptions would include welding in particularly large welded ignimbrite systems if the  
360 emplacement mode is *en masse* (we give the result for the  $L \leq 400 \text{ m}$  Bad Step Tuff, for  
361 which  $\bar{L}$  can exceed unity). However, under the assumption of the progressive-aggradation  
362 model for the sedimentation of ignimbrites (Branney and Kokelaar 1992) and an estimated,  
363 rising  $L \approx 2 \text{ m}$  thick welding window (Andrews and Branney 2011), we find that  $\bar{L} \ll 1$  is  
364 more typical for ignimbrite emplacement. The *en masse* and progressive aggradation models  
365 for ignimbrite emplacement represent upper and lower bounds on  $\bar{L}$ , respectively.



366 We also find that volcanic welding scenarios span the  $\bar{P} = 1$  divide, implying that  
367 there are cases for which pressure welding dominates ( $\bar{P} > 1$ ) and cases for which capillary  
368 welding dominates ( $0 \leq |\bar{P}| < 1$ ). Pressure welding appears to be typical of tuffisites and  
369 ignimbrites, while capillary welding appears to be typical of the formation of obsidian  
370 pyroclasts and of undesirable welding in the combustion chamber of jet engines (Figure 5).  
371 Tuffisites, in particular, are known to have variable and complex pressure–temperature  
372 histories, implying that they may track through  $\bar{P}$  space during their formation and welding  
373 (Tuffen and Dingwell 2005; Castro et al. 2012; Saubin et al. 2016). If the exact evolution of  
374 pressure and temperature were known, then our model could be used to determine the degree  
375 of welding throughout.

376 For each of the cases presented in Figure 5, we can compute a timescale for the  
377 porosity to reach the equilibrium value  $\phi = \phi_c$ . For systems welding at any  $\bar{P}$ , for  $\bar{L} \ll 1$ ,  
378 this timescale includes contributions from the pressure and capillary components, and can be  
379 taken as the reciprocal of the sum of the characteristic welding rates associated with the  
380 confining pressure and capillary pressure terms

381

$$\lambda_W \approx \left( \frac{\Delta P}{\langle \mu \rangle} + \frac{\Gamma}{\langle \mu \rangle \langle R_i \rangle} \right)^{-1}. \quad \text{Eq. 8}$$

382

383 We use Eq. 8 and the inputs in Table 1 to compute  $\lambda_W$  (in seconds) for each case study  
384 example given. We find that most systems weld over a timescale of 1 second to 1 day.  
385 Exceptions, which require very long timescales to weld, are crystal-rich tuffisites (Kendrick  
386 et al. 2016) or obsidian pyroclasts welding under the lowest temperature and gas pressure  
387 conditions expected (Gardner et al. 2017). In both of those slow-welding scenarios, it is  
388 unlikely that welding will complete before other processes, such as cooling of the particles or

389 deposit, terminate welding. However, remarkably, the welding timescale for most rhyolitic  
390 systems investigated appears to span a similar range regardless of the  $\bar{P}$  of formation; hence  
391  $\langle\mu\rangle$ , and therefore the degassing and temperature history, is the most important controlling  
392 parameter in welding for rhyolitic magmas.

393

### 394 c. User-friendly computational tools for solving welding problems in volcanic 395 scenarios in Python™ and Excel™

396 As part of this contribution, we provide a downloadable executable file for Linux™ and Mac  
397 platforms, which solves the full diffusion–welding problem given here. The executable  
398 requires the following user inputs: particle size distribution (as a .txt or .csv file), initial  
399 porosity  $\phi_i$ , initial dissolved water concentration  $C_i$ , initial temperature, gas pressure  $P_g$ ,  
400 pressure differential  $\Delta P = P_l - P_g$ , surface tension  $\Gamma$ , and the spatial resolution for the  
401 diffusion solution (we set a default value of 100 steps, which is sufficient for most cases). We  
402 additionally allow the user to input a temperature rate, which should be positive for heating,  
403 negative for cooling, or zero for isothermal conditions, and which imposes a linear change in  
404 temperature. The outputs of this code are the monodisperse or polydisperse solutions for  
405 porosity as a function of time and the value of  $\langle C \rangle$ . Similarly, we provide an editable Excel™  
406 sheet for solving our welding code for isothermal or non-isothermal conditions including for  
407 polydisperse particles (or droplets), but without diffusion of volatiles. This code is available  
408 via VHub (<https://vhub.org/resources/4568>).

409

410

## 411 6. Concluding remarks

412 We present a universal theoretical model of welding of natural volcanic material at relevant  
413 volcanic conditions. The model includes the complex effect of syn-welding dehydration,

414 accounts for the effects of confining pressure and capillary pressure, and is valid for both  
415 isothermal and non-isothermal conditions. The welding model is grounded in the  
416 microphysical behaviour of a welding system, and requires no fitting parameters. We use  
417 scaling arguments to assess the validity of the model for natural welding scenarios, and  
418 conclude that it can be applied to welding in tuffisites, in volcanic conduits, [at the base of](#)  
419 [aggrading pyroclastic density currents](#), and in jet engines. The model therefore provides a  
420 flexible and general tool for investigating welding phenomena across a wide range of  
421 volcanically-relevant scenarios.

422

423

424 Acknowledgements

425 We acknowledge European Research Council Advanced Grant EVOKES 247076, UK NERC  
426 grants NE/N002954/1 and No. NE/M018687/1, a fellowship from the Institute of Advanced  
427 Study at Durham University (to J. Gardner) and from the Centre for Advanced Study at  
428 LMU, Munich (to F. Wadsworth), a Royal Society University Research Fellowship (to H.  
429 Tuffen) and Royal Society International Exchange grant (to H. Tuffen and M. Heap), and the  
430 VUELCO consortium funded under the EU's FP7 grant agreement 282759. The Paul-  
431 Scherer-Institute (Swiss Light Source) awarded beamtime under proposals No. 20141231 and  
432 No. 20150413 at the TOMCAT beamline. Thanks to Yan Lavallée and Jackie Kendrick for  
433 valuable discussions and for supporting J. Schauroth's contribution to this work. S.  
434 Wiesmaier is thanked for assistance on the beamline. All raw data are available on request  
435 from the authors. Codes available via VHub at <https://vhub.org/resources/4568>.

436

437 Author contributions to this work

438 The team at the TOMCAT beamline (PSI, Switzerland) included F.B. Wadsworth (team  
439 lead), J. Vasseur, E.W. Llewellyn, K.J. Dobson, F.W. von Aulock, J. Fife, and F. Marone. J.  
440 Schauroth and K.J. Dobson processed the 3D datasets and extracted raw data. F.B.  
441 Wadsworth, J. Vasseur, and E.W. Llewellyn performed the analysis and model development.  
442 F.B. Wadsworth, J. Schauroth, J.E. Gardner, K.-U. Hess, M.J. Heap, H. Tuffen, and D.B.  
443 Dingwell provided additional *ex situ* or calibration data for analysis and consulted on the data  
444 treatment and the manuscript. F.B. Wadsworth, J. Schauroth, and E.W. Llewellyn led the  
445 drafting of a manuscript text with help from all authors. T. Havard compiled data from  
446 natural deposits.

447

448

449 References cited

450

451

452 Andrews GDM, Branney MJ (2011) Emplacement and rheomorphic deformation of a large,

453 lava-like rhyolitic ignimbrite: Grey's Landing, southern Idaho. *Geol Soc Am Bull*

454 123:725–743. doi: 10.1130/b30167.1

455 Branney M, Kokelaar Bp, McConnell B (1992) The Bad Step Tuff: a lava-like rheomorphic

456 ignimbrite in a calc-alkaline piecemeal caldera, English Lake District. *Bull Volcanol*

457 54:187–199. doi: 10.1007/BF00278388

458 Branney M, Kokelaar P (1992) A reappraisal of ignimbrite emplacement: progressive

459 aggradation and changes from particulate to non-particulate flow during emplacement of

460 high-grade ignimbrite. *Bull Volcanol* 54:504–520. doi: 10.1007/BF00301396

461 Castro JM, Bindeman IN, Tuffen H, Ian Schipper C (2014) Explosive origin of silicic lava:

462 Textural and  $\delta D-H_2O$  evidence for pyroclastic degassing during rhyolite effusion. *Earth*

463 *Planet Sci Lett* 405:52–61. doi: 10.1016/j.epsl.2014.08.012

464 Castro JM, Cordonnier B, Tuffen H, et al (2012) The role of melt-fracture degassing in

465 defusing explosive rhyolite eruptions at volcán Chaitén. *Earth Planet Sci Lett* 333:63–

466 69. doi: <http://dx.doi.org/10.1016/j.epsl.2012.04.024>

467 Cimarelli C, Yilmaz T, Colombier M, et al (2017) Micro-and nano-CT textural analysis of an

468 experimental volcanic fulgurite. *EGU Gen Assem Conf Abstr* 19:17982

469 Clarke AB, Voight B (2000) Pyroclastic current dynamic pressure from aerodynamics of tree

470 or pole blow-down. *J Volcanol Geotherm Res* 100:395–412. doi: 10.1016/S0377-

471 0273(00)00148-7

472 Elam WT, Kerstein AR, Rehr JJ (1984) Critical properties of the void percolation problem

473 for spheres. *Phys Rev Lett* 52:1516

474 Fife JL, Rappaz M, Pistone M, et al (2012) Development of a laser-based heating system for

475 in situ synchrotron-based X-ray tomographic microscopy. *J Synchrotron Radiat* 19:352–

476 358

477 Frenkel J (1945) Viscous flow of crystalline bodies under the action of surface tension. *J*

478 *Phys* 9:385–391

479 Friedman I, Long W, Smith RL (1963) Viscosity and water content of rhyolite glass. *J*

480 *Geophys Res* 68:6523–6535

481 Gardner JE, Llewellyn EW, Watkins JM, Befus KS (2017) Formation of obsidian pyroclasts

482 by sintering of ash particles in the volcanic conduit. *Earth Planet Sci Lett* 459:252–263.

483 doi: 10.1016/J.EPSL.2016.11.037

484 Gardner JE, Wadsworth FB, Llewellyn EW, et al (2018) Experimental sintering of ash at

485 conduit conditions and implications for the longevity of tuffisites. *Bull Volcanol* 80:23.

486 doi: 10.1007/s00445-018-1202-8

487 Gardner JE, Wadsworth FB, Llewellyn EW, et al (2019) Experimental constraints on the

488 textures and origin of obsidian pyroclasts. *Bull Volcanol* 81:22. doi: 10.1007/s00445-

489 019-1283-z

490 Giachetti T, Gonnermann HM (2013) Water in volcanic pyroclast: Rehydration or incomplete

491 degassing? *Earth Planet Sci Lett* 369–370:317–332. doi: 10.1016/J.EPSL.2013.03.041

492 Giehl C, Brooker R, Marxer H, Nowak M (2016) An experimental simulation of volcanic ash

493 deposition in gas turbines and implications for jet engine safety. *Chem Geol*

494 Giordano D, Russell JK, Dingwell DB (2008) Viscosity of magmatic liquids: a model. *Earth*

495 *Planet Sci Lett* 271:123–134

496 Gonnermann HM, Manga M (2003) Explosive volcanism may not be an inevitable

497 consequence of magma fragmentation. *Nature* 426:432–435

498 Gottsmann J, Giordano D, Dingwell DB (2002) Predicting shear viscosity during volcanic

499 processes at the glass transition: a calorimetric calibration. *Earth Planet Sci Lett*

500 198:417–427

501 Grunder AL, Laporte D, Druitt TH (2005) Experimental and textural investigation of  
502 welding: effects of compaction, sintering, and vapor-phase crystallization in the rhyolitic  
503 Rattlesnake Tuff. *J Volcanol Geotherm Res* 142:89–104. doi:  
504 <http://dx.doi.org/10.1016/j.jvolgeores.2004.10.018>

505 Heap MJ, Farquharson JI, Wadsworth FB, et al (2015) Timescales for permeability reduction  
506 and strength recovery in densifying magma. *Earth Planet Sci Lett* 429:223–233. doi:  
507 10.1016/j.epsl.2015.07.053

508 Hess KU, Cordonnier B, Lavallee Y, Dingwell DB (2007) High-load, high-temperature  
509 deformation apparatus for synthetic and natural silicate melts. *Rev Sci Instrum*  
510 78:75102. doi: 10.1063/1.2751398

511 Hess KU, Dingwell DB (1996) Viscosities of hydrous leucogranitic melts: A non-Arrhenian  
512 model. *Am Mineral* 81:1297–1300

513 Hess KU, Dingwell DB, Webb SL (1995) The influence of excess alkalis on the viscosity of  
514 a haplogranitic melt. *Am Mineral* 80:297–304

515 Kendrick JE, Lavallée Y, Varley NR, et al (2016) Blowing off steam: Tuffisite formation as a  
516 regulator for lava dome eruptions. *Front Earth Sci* 4:. doi: 10.3389/feart.2016.00041

517 Kennedy BM, Wadsworth FB, Vasseur J, et al (2016) Surface tension driven processes  
518 densify and retain permeability in magma and lava. *Earth Planet Sci Lett* 433:116–124.  
519 doi: 10.1016/j.epsl.2015.10.031

520 Liu Y, Zhang Y, Behrens H (2005) Solubility of  $H_2O$  in rhyolitic melts at low  
521 pressures and a new empirical model for mixed  $H_2O$ – $CO_2$   
522 solubility in rhyolitic melts. *J Volcanol Geotherm Res* 143:219–235

523 Lu B, Torquato S (1992) Nearest-surface distribution functions for polydispersed particle  
524 systems. *Phys Rev A* 45:5530

525 Mackenzie JK, Shuttleworth R (1949) A phenomenological theory of sintering. *Proc Phys*

526 Soc Sect B 62:833

527 McIntosh IM, Llewellyn EW, Humphreys MCS, et al (2014) Distribution of dissolved water  
528 in magmatic glass records growth and resorption of bubbles. *Earth Planet Sci Lett*  
529 401:1–11. doi: 10.1016/j.epsl.2014.05.037

530 Michaut C, Bercovici D, Sparks RSJ (2009) Ascent and compaction of gas rich magma and  
531 the effects of hysteretic permeability. *Earth Planet Sci Lett* 282:258–267

532 Mueller SP, Helo C, Keller F, et al (2018) First experimental observations on melting and  
533 chemical modification of volcanic ash during lightning interaction. *Sci Rep* 8:1389. doi:  
534 10.1038/s41598-018-19608-3

535 Olevsky EA (1998) Theory of sintering: from discrete to continuum. *Mater Sci Eng R*  
536 Reports 23:41–100

537 Prado M, Dutra Zanotto E, Müller R (2001) Model for sintering polydispersed glass particles.  
538 *J Non Cryst Solids* 279:169–178

539 Prousevitch AA, Sahagian DL, Anderson AT (1993) Dynamics of diffusive bubble growth in  
540 magmas: isothermal case. *J Geophys Res Solid Earth* 98:22283–22307. doi:  
541 10.1029/93JB02027

542 Quane SL, Russell JK (2005a) Welding: insights from high-temperature analogue  
543 experiments. *J Volcanol Geotherm Res* 142:67–87. doi:  
544 <http://dx.doi.org/10.1016/j.jvolgeores.2004.10.014>

545 Quane SL, Russell JK (2005b) Ranking welding intensity in pyroclastic deposits. *Bull*  
546 *Volcanol* 67:129–143

547 Riehle JR (1973) Calculated Compaction Profiles of Rhyolitic Ash-Flow Tuffs. *Bull Geol*  
548 *Soc Am* 84:2193–2216. doi: 10.1130/0016-7606(1973)84<2193:CCPORA>2.0.CO;2

549 Russell JK, Quane SL (2005) Rheology of welding: inversion of field constraints. *J Volcanol*  
550 *Geotherm Res* 142:173–191. doi: <http://dx.doi.org/10.1016/j.jvolgeores.2004.10.017>



551 Rust AC, Cashman K V, Wallace PJ (2004) Magma degassing buffered by vapor flow  
552 through brecciated conduit margins. *Geology* 32:349–352

553 Ryan AG, Russell JK, Nichols ARL, et al (2015) Experiments and models on H<sub>2</sub>O retrograde  
554 solubility in volcanic systems. *Am Mineral* 100:774–786. doi: 10.2138/am-2015-5030

555 Saubin E, Tuffen H, Gurioli L, et al (2016) Conduit Dynamics in Transitional Rhyolitic  
556 Activity Recorded by Tuffisite Vein Textures from the 2008–2009 Chaitén Eruption.  
557 *Front Earth Sci* 4:. doi: 10.3389/feart.2016.00059

558 Sparks RSJ, Tait SR, Yanev Y (1999) Dense welding caused by volatile resorption. *J Geol*  
559 *Soc London* 156:217–225. doi: 10.1144/gsjgs.156.2.0217

560 Streck MJ, Grunder AL (1995) Crystallization and welding variations in a widespread  
561 ignimbrite sheet; the Rattlesnake Tuff, eastern Oregon, USA. *Bull Volcanol* 57:151–169

562 Sumner JM, Branney MJ (2002) The emplacement history of a remarkable heterogeneous,  
563 chemically zoned, rheomorphic and locally lava-like ignimbrite: ‘TL’ on Gran Canaria.  
564 *J Volcanol Geotherm Res* 115:109–138. doi: 10.1016/S0377-0273(01)00311-0

565 Tuffen H, Castro JM (2009) The emplacement of an obsidian dyke through thin ice:  
566 Hrafninnuhryggur, Krafla Iceland. *J Volcanol Geotherm Res* 185:352–366

567 Tuffen H, Dingwell D (2005) Fault textures in volcanic conduits: evidence for seismic trigger  
568 mechanisms during silicic eruptions. *Bull Volcanol* 67:370–387. doi: 10.1007/s00445-  
569 004-0383-5

570 Tuffen H, Dingwell DB, Pinkerton H (2003) Repeated fracture and healing of silicic magma  
571 generate flow banding and earthquakes? *Geology* 31:1089–1092. doi: 10.1130/g19777.1

572 Vasseur J, Wadsworth FB (2017) Sphere models for pore geometry and fluid permeability in  
573 heterogeneous magmas. *Bull Volcanol* 79:. doi: 10.1007/s00445-017-1165-1

574 Vasseur J, Wadsworth FB, Lavallée Y, et al (2013) Volcanic sintering: Timescales of viscous  
575 densification and strength recovery. *Geophys Res Lett* 40:5658–5664. doi:

576 10.1002/2013GL058105

577 Wadsworth FB, Vasseur J, Aulock FW, et al (2014) Nonisothermal viscous sintering of  
578 volcanic ash. *J Geophys Res Solid Earth* 119:8792–8804

579 Wadsworth FB, Vasseur J, Llewellyn EW, et al (2016) Sintering of viscous droplets under  
580 surface tension. *Proc R Soc A Math Phys Eng Sci* 472:20150780. doi:  
581 10.1098/rspa.2015.0780

582 Wadsworth FB, Vasseur J, Llewellyn EW, et al (2017a) Topological inversions in coalescing  
583 granular media control fluid-flow regimes. *Phys Rev E* 96:. doi:  
584 10.1103/PhysRevE.96.033113

585 Wadsworth FB, Vasseur J, Llewellyn EW, Dingwell DB (2017b) Sintering of polydisperse  
586 viscous droplets. *Phys Rev E* 95:033114. doi: 10.1103/PhysRevE.95.033114

587 Walker GPL (1983) Ignimbrite types and ignimbrite problems. *J Volcanol Geotherm Res*  
588 17:65–88. doi: 10.1016/0377-0273(83)90062-8

589 Wright HM, Cashman K V (2014) Compaction and gas loss in welded pyroclastic deposits as  
590 revealed by porosity, permeability, and electrical conductivity measurements of the  
591 Shevlin Park Tuff. *Geol Soc Am Bull* 126:234–247. doi: 10.1130/b30668.1

592 Zhang Y, Ni H (2010) Diffusion of H, C, and O components in silicate melts. *Rev Mineral*  
593 *Geochemistry* 72:171–225

594

**Table 1** Constraints underpinning  $\bar{P}$  and  $\bar{L}$  from natural deposits or scenarios

	Particle viscosity <sup>#</sup> $\mu$ (Pa.s)	System length $L$ (m)	Particle radius <sup>§</sup> $R_i$ (m)	Liquid pressure $P_l$ (Pa)	Gas pressure $P_g$ (Pa)	Initial water content** $C_i$ (wt.%)	Emplacement temperature** $T$ (K)	References
<b>Welded ignimbrites</b>								
Bad Step Tuff	$10^7$ - $10^8$	40-400*	$10^5$ - $10^3$	$10^6$ - $10^7$	$10^5$ - $10^6$	0.1-0.2	1273	(Branney et al. 1992)
TL	$10^5$ - $10^6$	10.4-28*	$10^5$ - $10^3$	3.1-7.5x10 <sup>5</sup>	$10^5$ - $10^6$	0.47-0.87	1084-1183	(Sumner and Branney 2002)
Grey's Landing	$10^7$ - $10^9$	2-70*	$10^5$ - $10^3$	$10^5$ - $10^6$	$10^5$ - $10^6$	0.1-0.2	1198-1298	(Andrews and Branney 2011)
Rattlesnake tuff	$10^8$ - $10^{10}$	15-70*	$10^5$ - $10^3$	4.1x10 <sup>5</sup> -10 <sup>6</sup>	$10^5$ - $10^6$	0.1-0.2	1073-1153	(Streck and Grunder 1995)
<b>Tuffsites</b>								
Chaitén (2008)	$10^7$ - $10^9$	0.005-0.03	1.25x10 <sup>-4</sup> - 2.5x10 <sup>-4</sup>	$10^6$ - $10^7$	4.6x10 <sup>6</sup> - 8.1x10 <sup>6</sup>	0.44-1.2	1023-1098	(Castro et al. 2012; Saubin et al. 2016)
Cordon Caulle 2011- 2013	$10^8$ - $10^9$	0.005-0.03	$10^6$ - $10^3$	$10^6$ - $10^7$	4.6x10 <sup>6</sup> - 8.1x10 <sup>6</sup>	0.16-0.25	1168	(Castro et al. 2014)
Colima	$10^{10}$ - $10^{11}$	0.001-0.05	$10^4$ - $10^3$	$10^5$ - $10^6$	$10^5$	0.1-0.2	1213-1253	(Kendrick et al. 2016)
Törfajökull	$10^9$ - $10^{14}$	0.001-0.05	$10^5$ - $10^3$	$10^6$ - $10^7$	4.6x10 <sup>6</sup> - 8.1x10 <sup>6</sup>			(Tuffen and Dingwell 2005)
<b>Obsidian pyroclasts</b>								
Mono craters	$10^6$ - $10^{12}$	0.01-0.02	2x10 <sup>-5</sup> - 1.7x10 <sup>-4</sup>	1.002x10 <sup>5</sup>	$10^5$			(Gardner et al. 2017)
<b>Jet engine deposits</b>								
Rhyolitic experimental	$10^3$ - $10^9$	$10^3$ - $10^2$	3x10 <sup>-5</sup>	4.0002x10 <sup>6</sup>	4x10 <sup>6</sup>	0.1	1148-1848	(Giehl et al. 2016)

<sup>#</sup>The viscosity is either taken from the references for each case study or otherwise is calculated using *Hess and Dingwell*, [1996] with the  $C_i$  and  $T$  given for most cases (exceptions are the TL ignimbrite and the basaltic example for the jet engine deposits, both of which are calculated using *Giordano et al.*, [2008] and the composition given in the references; for TL, we use the WTL trachyte zone composition because this is the 'lava like' facies (Sumner and Branney 2002)).

\*This system length is assuming *en masse* deposition, but for progressive aggradation we take 2 m for all ignimbrites

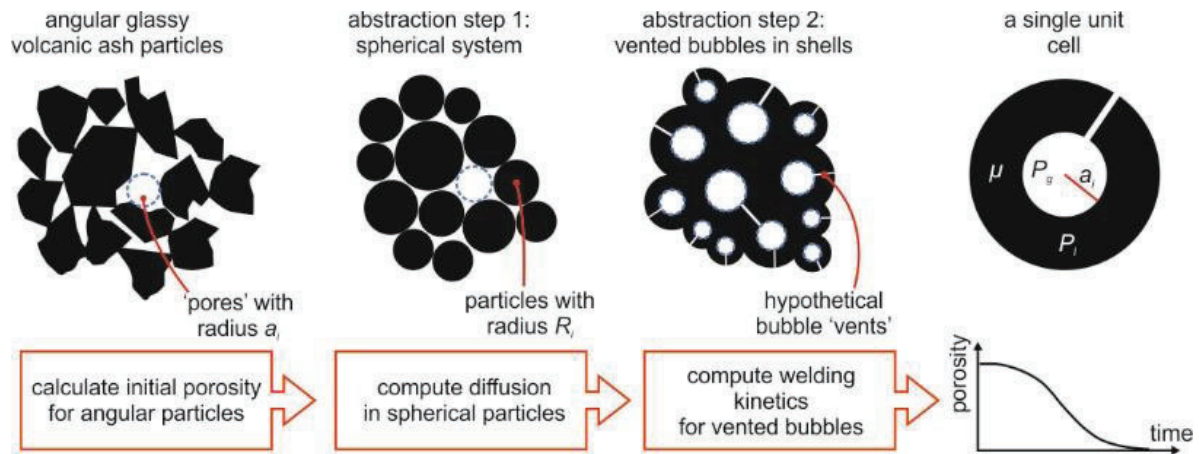
<sup>†</sup>We take this liquid pressure to be the hydrostatic loading pressure assuming a density of 2300 kg.m<sup>-3</sup>. Except for the tuffsite cases, the gas pressure is added to the liquid pressure.

<sup>‡</sup>The upper limit of these gas pressures is given by estimates of dynamic pressures during transport in pyroclastic density currents (Clarke and Voight 2000).

\*\*Note that these parameters are only required if the viscosity is not given directly by the originating authors. The value for  $C_i$  is approximated as 0.1-0.2 wt.% if other information is not given.

<sup>§</sup>We make the simplifying assumption that  $a_i = R_i$  for this scaling analysis.





597

598 **Figure 1.** The development of a diffusion–welding model. The natural system is composed of

599 angular volcanic particles, which are abstracted to a pack of spherical particles with the same

600 initial porosity. The diffusion model is used (Eq. 3) to compute the average water content as a

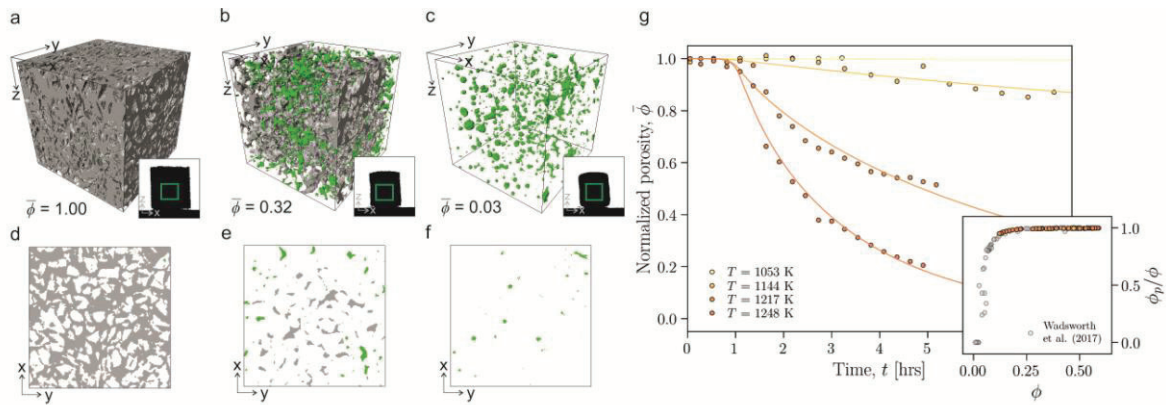
601 function of time  $\langle C \rangle(R_i, t)$ , which is converted to an average viscosity  $\langle \mu \rangle$ . Then we make a

602 further abstraction to vented bubble geometry and the welding is computed in terms of an

603 evolution of the total porosity with time  $\phi(t)$  using Eqs 1-2, accounting for the

604 polydispersivity of the initial particle size distribution (Wadsworth et al. 2017b).

605



606

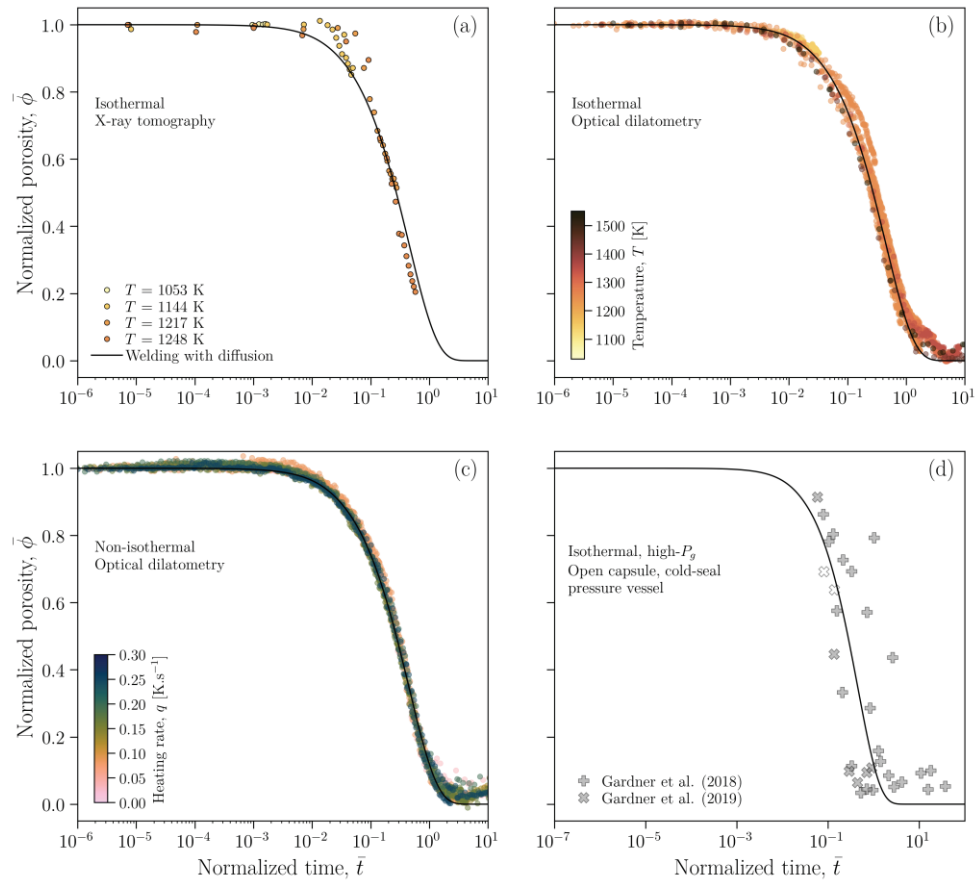
607 [Full page width]

608 **Figure 2.** Constraints of time-dependent welding collected *in situ* using either optical  
 609 dilatometry or x-ray tomography. **a-c**, 3-dimensional rendered images of the time-dependent  
 610 welding process segmented on the basis of grayscale gradient filtering from continuous, time-  
 611 resolved, *in situ* x-ray tomography data. The particle phase is rendered transparent, and the  
 612 pore phase is divided into a grey and a green component depending on whether it is  
 613 connected across the sample in any direction (grey) or is isolated from connections (green).  
 614 Box edge lengths of the sub-volume displayed are 350  $\mu\text{m}$ . Displayed is one representative  
 615 experiment performed at  $T = 1350 \text{ K}$ , for which the dimensionless porosity  $\bar{\phi}$  is labelled.  
 616 Inset in each panel is the 2-dimensional side-view of an initially cylindrical sample from an  
 617 experiment at the same conditions performed in the optical dilatometer (image base length of  
 618 5 mm). **d-f**, a 2-dimensional horizontal slice through each of the 3-dimensional rendered  
 619 images in **a-c** taken at the midpoint of the z-axis in the sample. **g**, The porosity as a function  
 620 of time of the obsidian particles sintered *in situ* using time-resolved x-ray tomography at a  
 621 range of temperatures (labelled). The curves represent the solutions to Eqs 1 or 2 with  $\bar{P} = 0$   
 622 and computing the time-dependent diffusion of volatiles out of the particles (Eq. 4). *Inset*: the  
 623 connectivity of the pore phase with porosity showing the collapse from fully connected to

624 isolated as  $\phi \rightarrow \phi_c$  during welding. Data are compared with welding in synthetic glass  
625 systems (Wadsworth et al. 2017a).

626

627



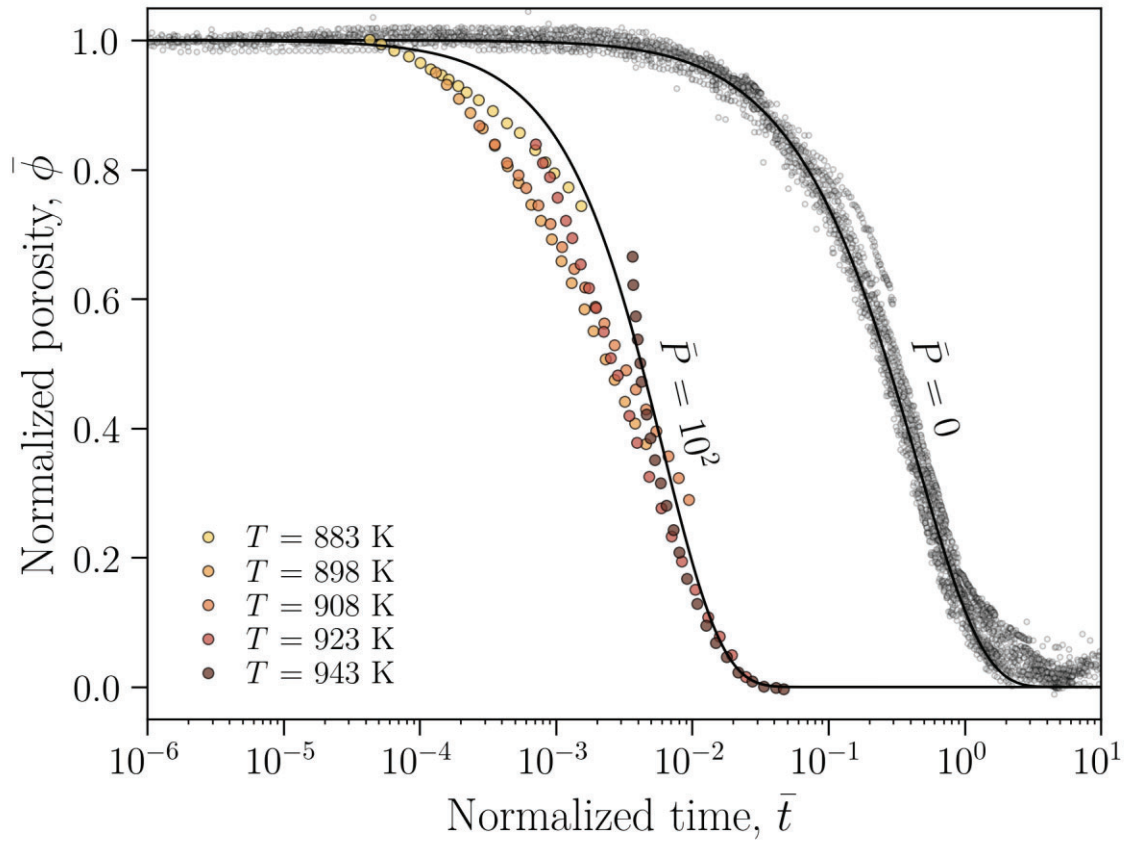
628

629 [full page width]

630 **Figure 3.** Modeling the evolution of the pore phase between the welding droplets. **a**, the  
 631 porosity  $\bar{\phi}$  as a function of time for each experimental  $T$  for the x-ray tomography  
 632 experiments only. These data are compared with the results of Eq. 2 (welding) with Eq. 4  
 633 (diffusion), which account for syn-welding degassing of the droplets and which require no  
 634 fitting parameters. These data are the same as those presented in Figure 2g. **b**, the same as **a**  
 635 but for the data collected using optical dilatometry (i.e. without 3-dimensiona  
 636 microstructural information) showing that this technique can be used to capture the bulk  
 637 decay of porosity with time. **c**, the same dimensionless plot as in **b** but for non-isothermal  
 638 experiments at different experimental heating rates, showing that regardless of the  $T(t)$  path  
 639 taken by the samples, the efficacy of our model (Eqs 4-6) is robust. In all panels, the  
 640 dimensionless time is given by Eq. 3. **d**, The data from Gardner et al. (2018) and Gardner et  
 641 al. (2019) collected using a high- $P_g$  cold seal vessel, re-analysed using the diffusion-welding



642 model given here. The filled points represent data for which rhyolite particles are hydrating  
643 (from  $C_i = 0.15$  wt.% to equilibrium conditions at high  $P_g$  and high  $T$ ) while welding, and  
644 the un-filled points represent data for which rhyolite particles are de-hydrating (from  
645  $C_i = 2.3$  wt.% to equilibrium conditions at high  $P_g$  and high  $T$ ). See the papers originating  
646 the data for more information.  
647



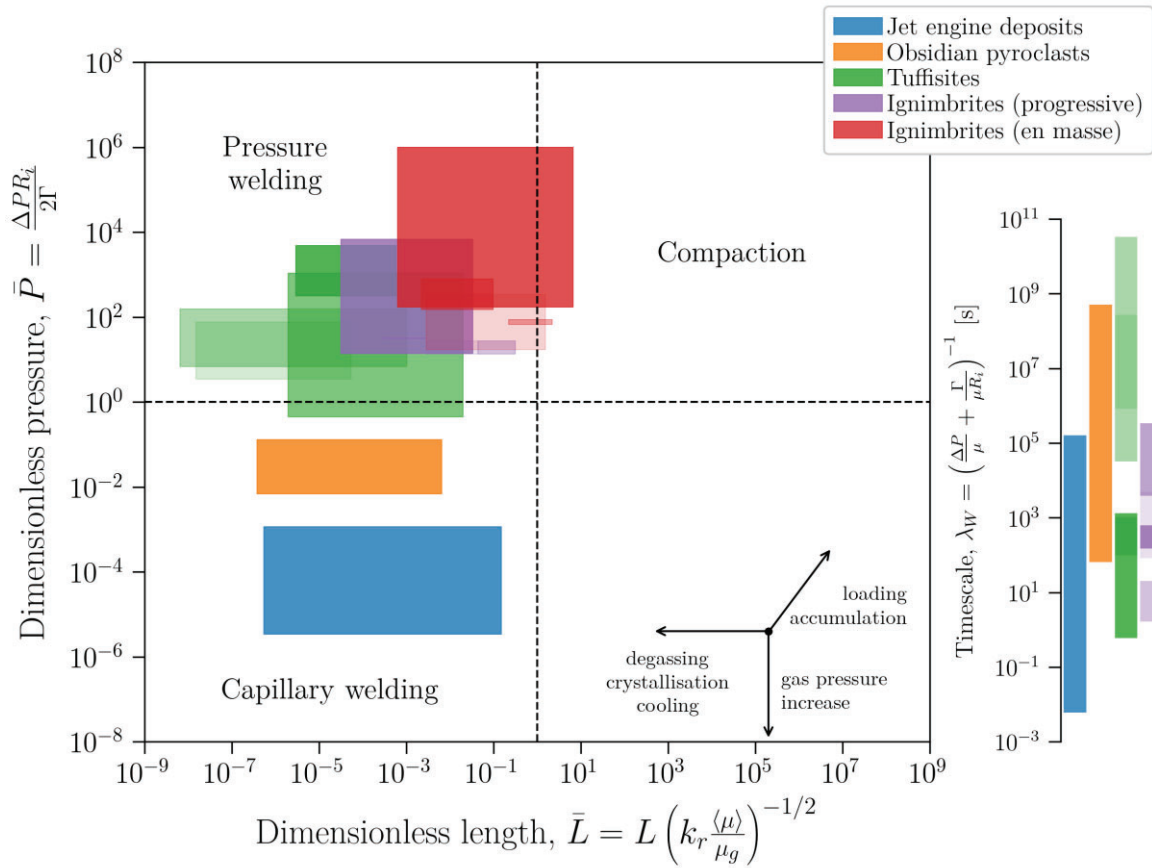
649

650 [half-page width or less]

651 **Figure 4.** The effect of pressure on the welding of glassy particles. Shown here are data from  
 652 *Friedman et al.*, [1963], in which synthetic glass particles (Pyrex™) are welded under a  
 653 pressure equivalent to  $\bar{P} = 100$ , and at a range of temperatures (labelled). We use the values  
 654 of  $\mu$ ,  $R_i$  and  $P_l$  given in their work, and the curve represents the solution to Eq. 2 without  
 655 fitting parameters. Shown for reference is the solution for  $\bar{P} = 0$  and all data from Figure 3  
 656 given in grey. In all cases, the dimensionless time is given by Eq. 3.

657

658



660

661

662 [1/2 page width or less]

663 **Figure 5.** Scenarios and regimes for volcanic welding. A plot of  $\bar{P}$  and  $\bar{L}$  regimes for volcanic

664 welding with the range of conditions for natural examples given using constraints compiled

665 in Table 1.

Figure 1  
Click here to download high resolution image

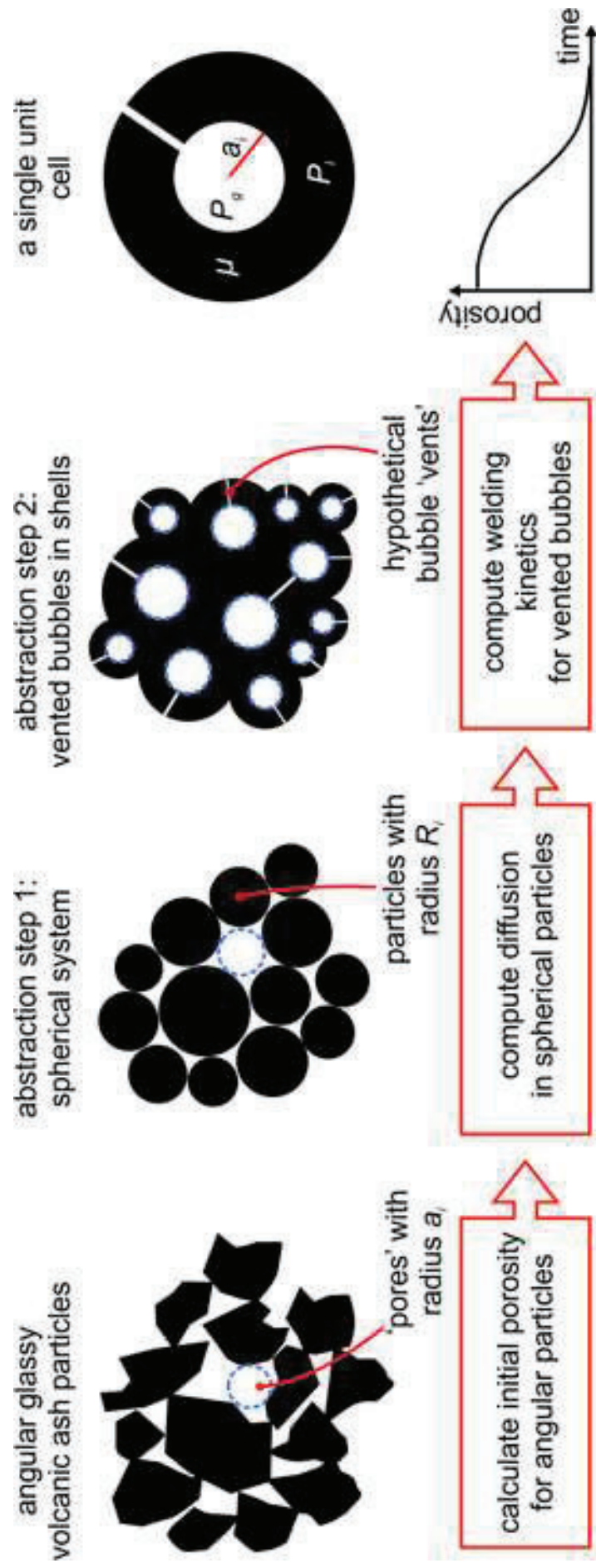


Figure 2  
Click here to download high resolution image

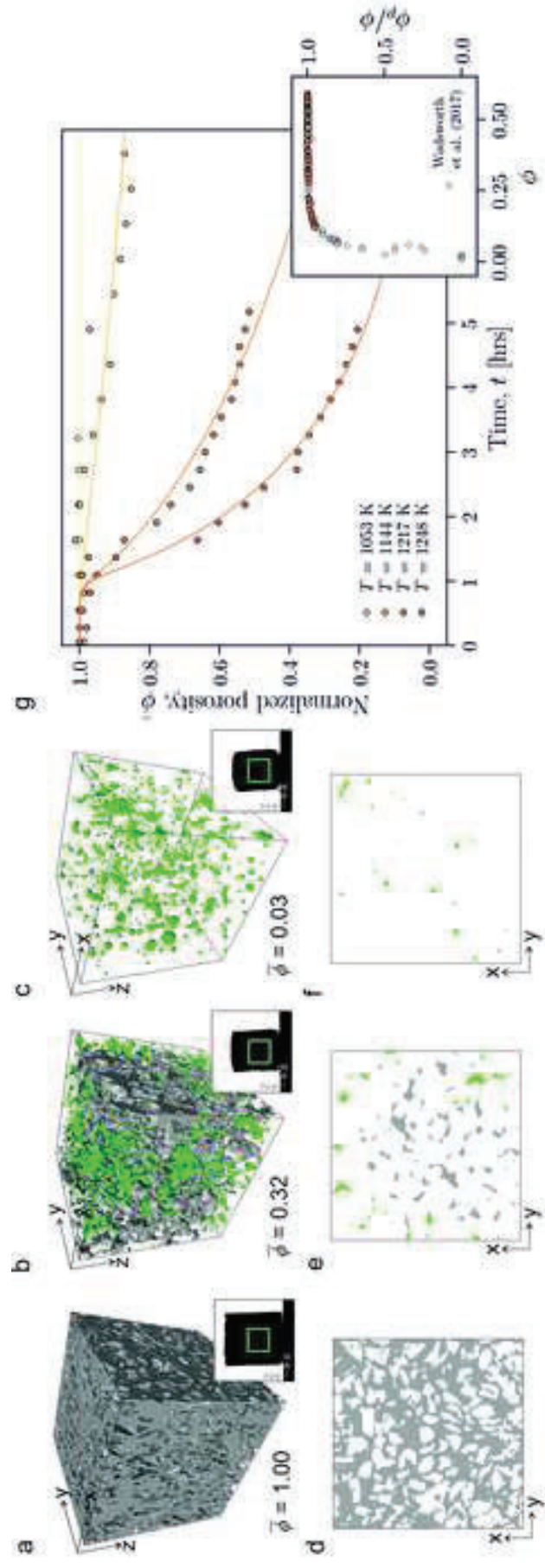


Figure 3  
[Click here to download high resolution image](#)

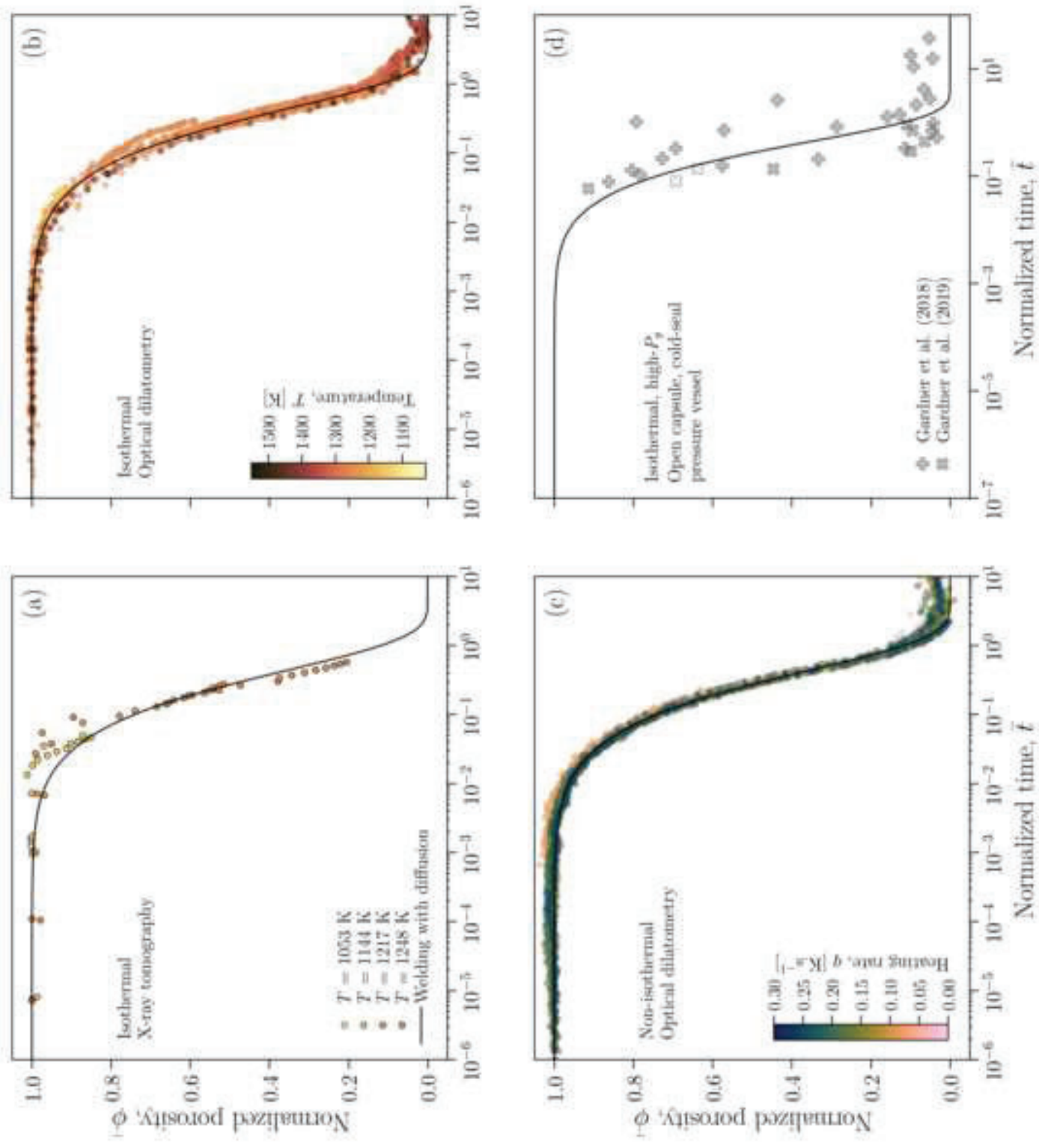


Figure 4  
[Click here to download high resolution image](#)

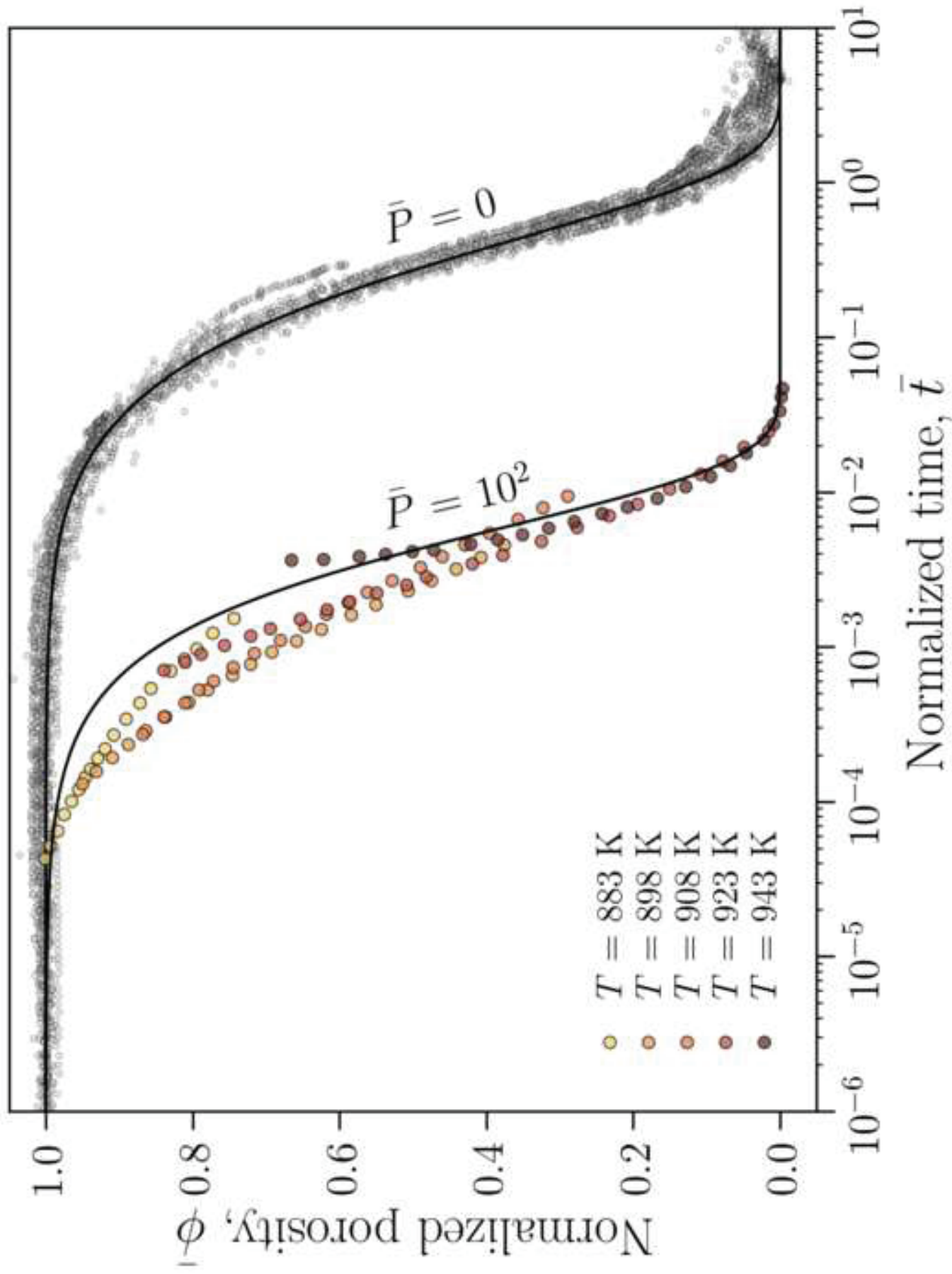
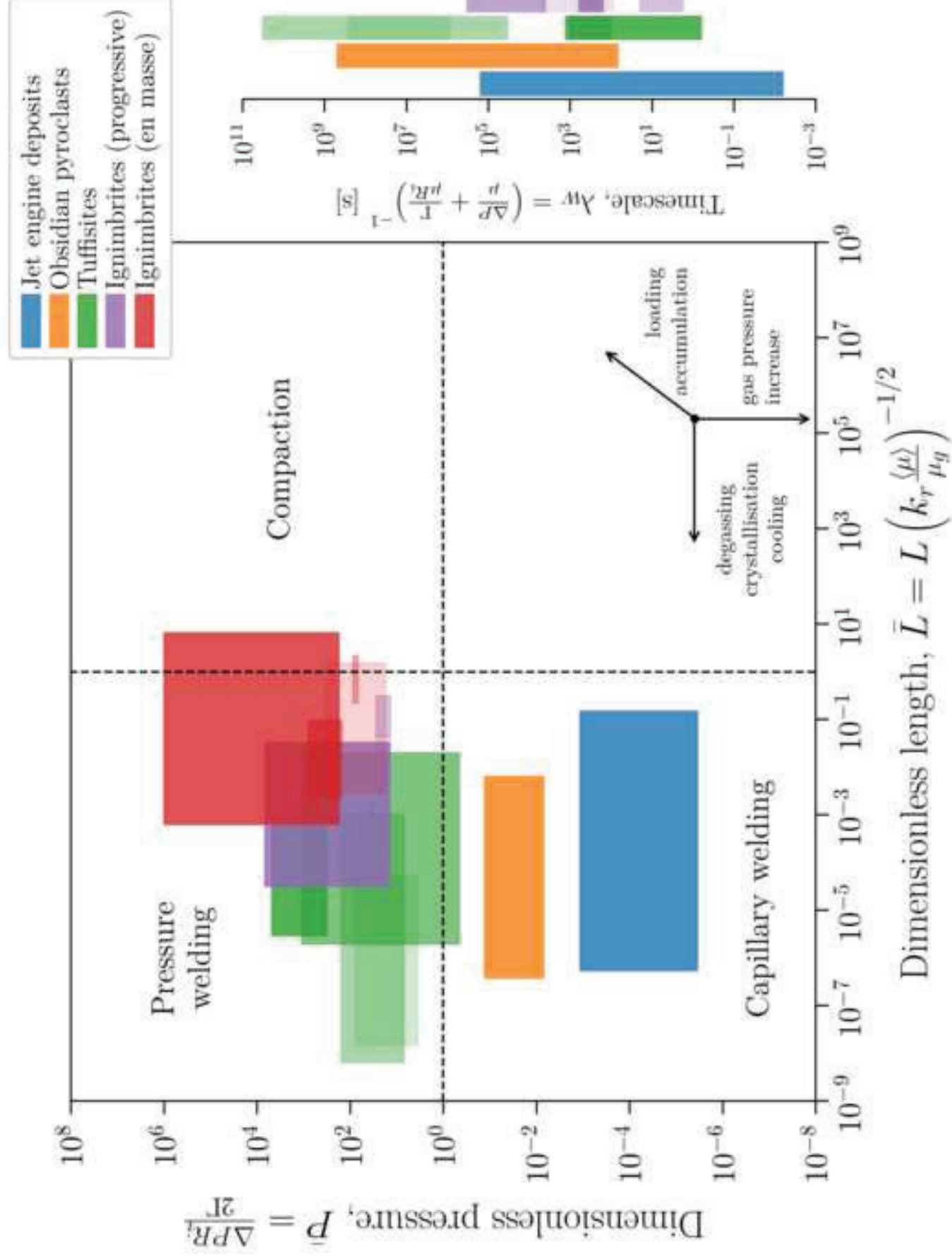


Figure 5  
[Click here to download high resolution image](#)





**Supplementary material for online publication only**

[Click here to download Supplementary material for online publication only: Supporting-Information\\_Wadsworth.docx](#)

Raw research data (under CC BY license; see above)

[Click here to download Raw research data \(under CC BY license; see above\): insitu\\_raw\\_data.txt](#)

Raw research data (under CC BY license; see above)

[Click here to download Raw research data \(under CC BY license; see above\): dilatometry\\_raw\\_data\\_non\\_iso.txt](#)

Raw research data (under CC BY license; see above)

[Click here to download Raw research data \(under CC BY license; see above\): dilatometry\\_raw\\_data\\_iso.txt](#)